

How glass breaks – Damage explains the difference between surface and fracture energies in amorphous silica

Gergely Molnár*

CNRS, INSA Lyon, LaMCoS, UMR5259, 69621 Villeurbanne, France

Etienne Barthel

Soft Matter Sciences and Engineering, CNRS, ESPCI Paris,
PSL University, Sorbonne Université, 75005 Paris, France

The difference between free surface energy and fracture toughness in amorphous silica is studied via multi-scale simulations. We combine the homogenization of a molecular dynamics fracture model with a phase-field approach to track and quantify the various energy contributions. We clearly separate free surface energy localized as potential energy on the surface and damage diffusion over a ca. 20 Å range around the crack path. The plastic contribution is negligible. These findings, which clarify brittle fracture mechanisms in amorphous materials, align with toughness measurements in silica.

Surface free energy quantifies the excess energy associated with unbalanced interatomic bonds at a material's surface. In solids, the bulk state is always energetically more favorable, so creating a surface requires energy input. Griffith [1] postulated a similar concept in his theory of crack propagation, stating that a crack can advance if the elastic energy released exceeds a material-specific threshold. Essentially, both free surface energy and fracture surface energy describe the same underlying phenomenon.

However, in experiments, fracture surface energy is almost always significantly higher. It is the case for polymers [2, 3] and crystalline metals [4] where the difference between free surface and fracture energies are found to span several orders of magnitude, because of plastic dissipation around the crack tip, and also for bulk metallic glasses [5, 6]. One of the rare exceptions is silicon crystals [7–9], where the difference falls within the precision limits of the methods used, and which can be assumed to break by individual bond rupture at an atomically sharp tip as expected from a brittle material [10].

Intriguingly, for silicate glasses, the archetypes of brittle materials, it has long been known that the measured fracture energy exceeds the surface free energy by a factor of ca. 5 [11–13]. The difference has been tentatively ascribed to plastic dissipation [11, 14] but as it is difficult to experimentally evidence plasticity at this scale in an amorphous material, let alone quantify it (and also because it openly conflicts with the accepted notion of brittleness), the claim has remained controversial [15] to these days: signs of plasticity at silica crack tips have been discounted [16] almost as soon as found [17]. Worse still, standard models for plastic dissipation in cracks [18] are inapplicable to silicates because their plasticity is essentially devoid of hardening [19].

Faced with this conundrum, we focused on silica glass to investigate the rupture of brittle amorphous materials at the crossover between the atomic and the continuum scales. Previous atomic scale simulations have recog-

nized the existence of an inelastic zone around the crack tip [20, 21]. Here, we show that we can clearly separate the two contributions to the fracture energy : 1) the energy required for surface formation—accounting for bond breaking and atomic relaxation near the surface—, and 2) the energy due to structural rearrangements extending much deeper into the material, over a distance of approximately 20 Å. We also show that the latter process is best described as damage rather than plasticity or nonlinear elasticity and that the ratio between the two contributions conforms to the experiments. This approach offers a fully consistent framework for understanding fracture in a model amorphous brittle material.

Simulation methods.— To explore the fracture properties of amorphous silica, the atomistic simulations employed the BKS potential [22] to model atomic interactions and Wolf's truncation method to handle Coulombic forces [23]. The BKS potential was shown to qualitatively but consistently describe the elastic and plastic mechanical properties of these systems [24, 25]. Amorphous glass samples were generated by randomly distributing atoms within a periodic box. Molecular dynamics simulations were then performed to equilibrate, quench, and test the samples. Athermal deformations, pertinent for systems below the glass transition temperature, were applied through iterative energy minimization using the conjugate gradient method. Further simulation details can be found in the Supplementary Materials.

Diffuse damage.—Fracture simulations were carried out on a 3D sample with dimensions $L_x \times L_y \times L_z = 400 \times 300 \times 100 \text{ \AA}^3$, containing 800k atoms, which was found to be large enough to capture initiation and propagation adequately (Fig. 1). The initial defect, a rounded incision with a radius of $r_c = 10 \text{ \AA}$ extends along the z direction on a face normal to the x direction. There is periodicity in the z direction. For the boundary conditions on the x and y faces, a K-field displacement was imposed, simulating uniaxial tension along y at infinity. The crack then initiated and propagated along the x direction as the

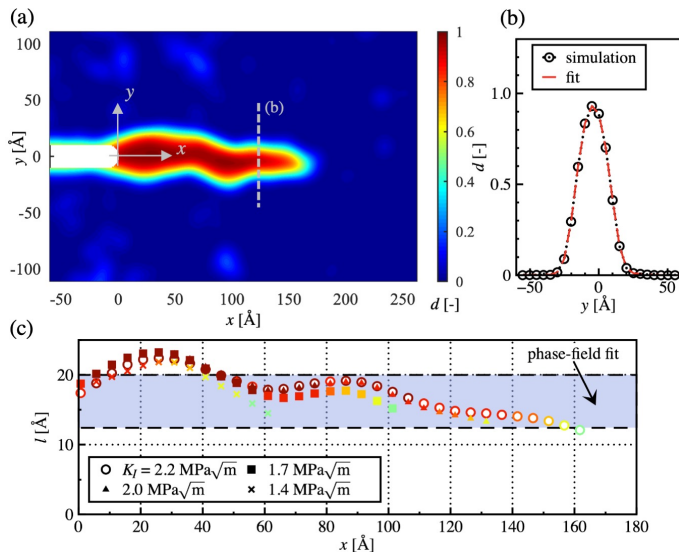


FIG. 1: Damage field obtained from molecular simulations: (a) Distribution of damage in the middle plane of the sample. (b) Circles represent the damage profile along the y direction at $x = 125$ Å, fitted with a Gaussian function of maximum height d_{\max} and width l . (c) Variation of the fitted width l along the crack and under different global loading states, color-coded by d_{\max} according to the colorbar. The blue region indicates l_c identified using the Finite Element Update (FEMU) scheme based on the phase-field formulation (see eq. 4).

loading parameter (K_I) was increased. Further details of the fracture simulation are available in the Supplementary Material.

The atomic scale fields of the cracked sample were then coarse-grained (CG), which essentially involves Gaussian convolution to ensure mass and energy conservation during the discrete-continuum transition. The choice of the CG width w will be discussed in detail below. As a result, the following continuum quantities were available in both Lagrangian and Eulerian configurations: displacements u , Hencky (logarithmic) strain tensor ε , Cauchy stress tensor σ , potential energy density ψ_{pot} (sum of the atomic interactions) and mass density ρ .

Under the assumption of linear elasticity, we can calculate the elastic strain energy density field [26] as

$$\psi_\varepsilon = \psi_{\varepsilon,0} + \int_{\varepsilon_0}^{\varepsilon} \sigma : d\varepsilon \approx \psi_{\varepsilon,0} + \frac{1}{2} \sigma : \varepsilon J, \quad (1)$$

where J denotes the determinant of the deformation gradient tensor, accounting for volume changes, and $\psi_{\varepsilon,0}$ is the initial strain energy density, which may be non zero, typically after quenching.

In the case of purely elastic deformation, the local elastic energy density field ψ_ε is equal to the undamaged strain energy ψ_0 calculated from the strain and the initial

local elastic stiffness. In contrast, our results evidence a dramatic reduction of the local elastic energy density ψ_ε over a large area surrounding the crack faces. This result is evidence for a significant evolution of the structure of the material around the crack tip.

To quantify this evolution, we resort to the continuum mechanics concept of damage, where the local material stiffness decreases gradually down to a vanishing stiffness which signals fracture [27]. Damage can thus conveniently be described as a scalar field defined by:

$$\psi_\varepsilon(\mathbf{u}, d) = (1 - d)^2 \psi_0(\varepsilon(\mathbf{u})). \quad (2)$$

Thus d evolves between 0 for the pristine and 1 for the fully damaged material. We have used the spectral energy decomposition scheme [28], i.e., the energy is calculated based on the principal values of the strain tensor, thereby preventing crack opening under compression. However, here, the compressive term is negligible and has been omitted from eq. (2). The detailed calculation can be found in the Supplementary Material.

Fig. 1a illustrates the damage distribution from molecular simulations in an xy plane slice of the simulation box after fracture propagation over ca., 150 Å. Fig. 1b shows a cross section along y at $x = 125$ Å with a Gaussian fit from which the damage width l is derived. Finally, Fig. 1c presents the damage width l along the crack. The width varies but typically equals 20 Å along the crack faces. The color map indicates maximum damage values along the y axis. Of course, for consistency, the CG width w must be kept small compared to the width of the damage zone l . As shown in detail in the Supplementary Material, we found that for $w = 3-5$ Å, the mean value of l remains the same, with only the fluctuation decreasing. At $w = 8$ Å, the mean value starts to increase slightly, but this increase remains within the order of 10%. As w increases beyond 8 Å, the width of the damage zone, l , increases linearly with w . The value $w = 8$ Å will be used subsequently.

The coarse-grained MD simulations demonstrate that damage around the crack is diffused rather than localized, extending into the material beyond the immediate crack tip. The diffusion width l is notably larger than the CG width used to transition from atomic to continuum scales, indicating that the CG width is sufficient to capture local damage and small enough to expose the actual physical spread of damage. Specifically, for fully opened cracks, the damage zone varies in width between approximately 16 and 23 Å, reflecting a non-uniform distribution of damage that suggests its extent may be influenced by structural heterogeneities. This local variability implies that the characteristic length of damage is small enough to depend on the structural heterogeneity rather than a continuum scale response.

Finite element scheme.— To show how the MD results can be fed into a continuum scale description, the damage

field was then recalculated using a Finite Element Update (FEMU) scheme on 20 slices of the sample to capture the variation along the thickness. During this process, the fracture toughness g_c and a constant damage width l_c were fitted to minimize the differences between the damage values obtained from coarse-grained molecular scale simulations and those calculated through a phase-field approach [29]. We assumed that the undamaged strain energy density ψ_0 is known at the atomic scale and minimized the internal energy of the system expressed as:

$$\Psi_{\text{int}}(\mathbf{u}, d) = \int_V \psi_\epsilon(\mathbf{u}, d) dV + g_c \Gamma(d, \nabla d), \quad (3)$$

where Γ represents the crack surface. In the phase-field approach [30], it is approximated using a crack density function (γ_Γ):

$$\Gamma = \int_V \gamma_\Gamma(d, \nabla d) dV = \frac{3}{8l_c} \int_V (d + l_c^2 |\nabla d|^2) dV. \quad (4)$$

Details are provided in the Supplementary Material.

Interestingly, the FEMU produced a damage width l_c ranging from 12 to 20 Å, depending on the loading state. This result correlates well with the observed coarse-grained damage width, even though l_c is treated as a global parameter in the FEMU. This correlation suggests that, while damage diffusion is locally variable, the global parameter l_c effectively captures the average behavior of the damage width.

In the literature, crack length is often calculated based on an assumed position of the crack tip, either from local density or using a singular Williams series fit. These methods are not sufficiently precise to describe the moving crack. Furthermore, they cannot capture multiple crack fronts. Here the FEMU approach provides a first method to determine the crack length which overcomes these drawbacks.

Free surface energy.—The free surface energy was determined using a smaller cubic sample with a side length of 100 Å. We slice the sample in half by removing atomic bonding along a plane, thus replacing the periodic boundary condition in the direction normal to the plane with a free surface. The mechanical equilibrium of this dissected sample was then reached through potential energy minimization. The free surface energy, 2γ , was calculated by dividing the energy difference by the area of the newly exposed surface. Notably, 2γ was found to be independent of the sample size once it surpassed the 50 Å box length.

We determined $2\gamma = 2.8 \pm 0.2$ J/m². This value is somewhat larger than room temperature experimental measurements (≈ 0.5 J/m²) [11, 31, 32] but in agreement with calculated temperature variations [33] and correlates well with simulations using more sophisticated potentials [21].

We observed that after cutting, equilibrium is reached through atomic displacements localized within a few interatomic distances from the surface. This finding aligns well with experimental observations of surface relaxation in crystals, where an exponential decay over the first few atomic layers has been reported [34]. Detailed information regarding the nature of the energy changes is provided in the Supplementary Material.

For an elastic deformation, we expect the potential energy ψ_{pot} to equal the elastic energy ψ_ϵ defined by Eq. 1. Structural evolution however, which is typically not reached through elastic deformation, will be reflected in a variation in ψ_{pot} . We therefore introduce the difference denoted

$$\psi_{\text{FSE}} = \psi_{\text{pot}} - \psi_\epsilon. \quad (5)$$

Fig. 2a shows the distribution of ψ_{FSE} along the normal to the surface for the dissected sample. When the coarse-graining is omitted and the energy difference is instead calculated by averaging over 1 Å slices, a pronounced localized peak emerges, as expected for simple surface relaxation. After coarse-graining, the profile width of ψ_{FSE} is observed to be 8 Å, reflecting the convolution of the highly localized peak with the width w .

A coarse-grained profile for the cracked samples, taken along the line indicated in (b), is also shown. The two coarse-grained ψ_{FSE} distributions are similar. This observation suggests that the ψ_{FSE} calculated in the fractured sample is the energy change due to the formation of the free surface. It is primarily the result of the surface relaxation due to the loss of atomic connectivity and differs from the damage process shown previously that penetrates significantly deeper into the sample. This is why we refer to this quantity as the free surface energy (FSE) density. Fig. 2b depicts the free surface energy during crack propagation.

Since the energy localization is consistent across different sample conditions, it appears that the free surface energy $2\gamma = \int_{-\infty}^{+\infty} \psi_{\text{FSE}} dy$ should also be an effective measure for assessing the area of newly formed cracks. Fig. 2c displays crack length calculated from the global sample free surface energy Ψ_{FSE} divided by 2γ . It is compared with the crack length determined by the FEMU based on the damage approach eq. (4). The two measures are very consistent although the FSE length is smaller than the FEMU length. This agreement between the two methods validates the use of ψ_{FSE} as a reliable metric for quantifying crack propagation, providing an alternative to more traditional methods and offering precise measurements that align well with continuum-based models.

Global energy equilibrium.—As noted in the introduction, experimental measurements have shown that the free surface energy resulting from surface relaxation accounts for only approximately 20% of the energy required

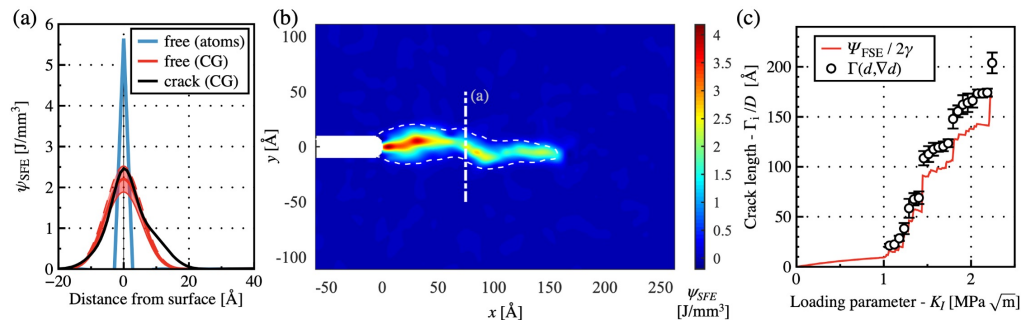


FIG. 2: (a) Profiles of free surface energy for different models. In color, values for the dissected sample are shown with discrete calculations and a CG width of 8 \AA . In black, results from the cracked and coarse-grained sample are shown at $x = 75$ \AA . (b) Free surface energy distribution at $K_I = 2.2 \text{ MPa}\sqrt{\text{m}}$. (c) Crack surface as a function of loading derived from Ψ_{FSE} and from phase-field calculations.

to open a crack. This section casts the free surface energy and the damage energy we have calculated at the atomic scale into a global energy balance to identify the origin of this discrepancy.

Fig. 3a illustrates the various energy contributions as a function of loading. The external work, W_{ext} , is partitioned into several components: the elastic strain energy, Ψ_ϵ , and the free surface energy (FSE), Ψ_{FSE} , whose sum is represented as Ψ_{pot} . Additionally, there is a small non-linear contribution, Ψ_{etc} , and a significant unquantified remainder. The non-linear energy contribution is determined by isolating the portion of the elastic energy density that exceeds the local potential energy, which ideally remains positive under the assumption of linear elasticity. This excess energy contribution, is then subtracted from the total elastic energy. However, it is noteworthy that this contribution (represented by the dashed line) is minor. This observation suggests that energy dissipation due to plasticity or ring folding is indeed negligible. Under tensile loading followed by fracture, these mechanisms contribute only marginally to the overall energy dissipation within the material.

The difference between the external work and the elastic strain energy $W_{\text{ext}} - \Psi_\epsilon$ can be interpreted as the total dissipation caused by fracture, denoted as Ψ_d . This dissipated energy is shown in Fig. 3b (solid red curve) and compared to the dissipation derived from the FEMU fit through eq. 3. Although the two methods are very different (the FEMU does not incorporate explicit knowledge of the external work), they provide very consistent results, highlighting the robustness of the determination of the total energy dissipation. Also shown in the same graph is the FSE, which clearly constitutes only a portion of the total dissipation.

Finally, Fig. 3c presents the fracture toughness (g_c) as a function of loading, calculated using three distinct methods: the J integral based on the coarse-grained stress and displacement fields (red filled circles – detailed calculations provided in the Supplementary Materials),

the FEMU phase-field fit (open circles) and the energy balance approach ($\Psi_d/\Gamma_{\text{FSE}}$) obtained from the coarse-grained atomic scale simulations. The initial linear increase follows from the crack initiation process. Subsequently, the fracture surface energy remains consistent across the three calculation methods. The resulting value provides a ratio of $2\gamma/g_c \approx 23\%$: this value found at the atomic scale is consistent with experimental findings [11].

Conclusions.—This Letter sheds new light on the origin of fracture toughness in brittle materials. We investigated the underlying mechanisms that explain the difference between free surface energy and fracture toughness in amorphous silica at the crossover between the atomic and the continuum scales. Using a combination of molecular dynamics and phase-field modeling, we quantified the different contributions to the energy dissipation that occurs during fracture. From a comprehensive energy balance analysis, we were able to clearly isolate the free surface energy term and identify an additional contribution resulting from damage, not plastic deformation. This damage contribution exceeds the free surface energy by a factor of about 4, in agreement with the experimental measurements.

These findings highlight that traditional notions of fracture in brittle materials often overlook the subtle nature of mechanical dissipation in fracture of amorphous materials. In particular they emphasize the dominant contribution of diffused damage in silicate glasses, aligning with experimental observations. Metallic glasses, which are known to span the transition from brittle to ductile fracture through clearly identified mechanostructural parameters [35] open an interesting perspective for more insight. It offers a more nuanced perspective for future materials design, particularly in optimizing the mechanical properties of brittle materials like silicates.

This research was funded, in part, by French Research National Agency program GaLAA D (ANR-20-CE08-0002).

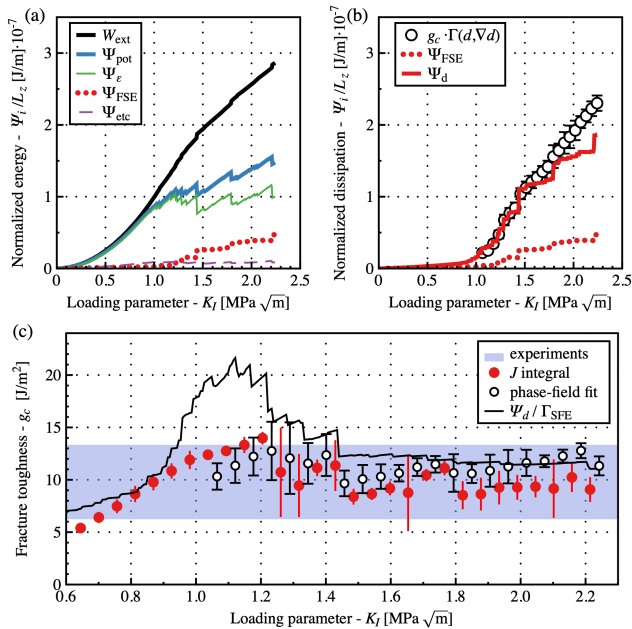


FIG. 3: Energy balance of the cracked sample as a function the loading parameter ^a. (a) Various energy contributions normalized by the thickness (L_z): external work (W_{ext}), potential energy (Ψ_{pot}), elastic strain energy (Ψ_ϵ), surface free energy (Ψ_{SFE}), and other unquantified contributions (plasticity, folding). (b) Dissipation calculated from the energy balance (Ψ_{d}) and crack surface energy from phase-field calculations. (c) Fracture toughness calculated using various methods.

^a We note that K_I loses its precise physical significance as the tip advances and must be considered as a mere loading parameter.

* gergely.molnar@insa-lyon.fr

[1] A. A. Griffith, Philosophical Transactions of the Royal Society of London A: Mathematical, Physical and Engineering Sciences **221**, 163 (1921).
 [2] K. Tokuda, T. Ogino, M. Kotera, and T. Nishino, Polymer journal **47**, 66 (2015).
 [3] T. Smith, C. Gupta, Z. Fan, G. J. Brust, R. Vogelsong, C. Carr, and S.-Q. Wang, Extreme Mechanics Letters **56**, 101819 (2022).
 [4] J. J. Bikerman, in *Inorganic and Physical Chemistry* (1978) pp. 1–66.
 [5] J. Xu, U. Ramamurty, and E. Ma, Jom **62**, 10 (2010).
 [6] P. Yiu, W. Diyatmika, N. Bönninghoff, Y.-C. Lu, B.-Z. Lai, and J. P. Chu, Journal of Applied Physics **127**, 030901 (2020).
 [7] J. J. Gilman, Journal of Applied Physics **31**, 2208 (1960).

[8] R. Pérez and P. Gumbsch, Phys. Rev. Lett. **84**, 5347 (2000).
 [9] D. J. Eaglesham, A. E. White, L. C. Feldman, N. Moriya, and D. C. Jacobson, Phys. Rev. Lett. **70**, 1643 (1993).
 [10] P. Gumbsch, Journal of Materials Research **10**, 2897 (1995).
 [11] S. M. Wiederhorn, J. Am. Ceram. Soc. **52**, 99 (1969).
 [12] S. K. Rhee, Journal of Materials Science **12**, 823 (1977).
 [13] G. D. Quinn and J. J. Swab, Journal of the European Ceramic Society **37**, 4243 (2017).
 [14] D. Marsh, Proceedings of the Royal Society of London. Series A. Mathematical and Physical Sciences **282**, 33 (1964).
 [15] B. R. Lawn, B. J. Hockey, and S. M. Wiederhorn, Journal of Materials Science **15**, 1207 (1980).
 [16] J.-P. Guin and S. M. Wiederhorn, Phys. Rev. Lett. **92**, 215502 (2004).
 [17] F. Célerié, S. Prades, D. Bonamy, L. Ferrero, E. Bouchaud, C. Guillot, and C. Marliere, Phys. Rev. Lett. **90**, 075504 (2003).
 [18] Y. Wei and J. W. Hutchinson, Int. J. Fract. **95**, 1 (1999).
 [19] G. Kermouche, G. Guillonneau, J. Michler, J. Teisseire, and E. Barthel, Acta Mater. **114**, 146 (2016).
 [20] C. Rountree, S. Prades, D. Bonamy, E. Bouchaud, R. Kalia, and C. Guillot, Journal of Alloys and Compounds **434-435**, 60 (2007).
 [21] J. M. Rimsza, R. E. Jones, and L. J. Criscenti, Journal of the American Ceramic Society **101**, 1488 (2018).
 [22] X. Yuan and A. N. Cormack, Journal of Non-Crystalline Solids **283**, 69 (2001).
 [23] A. Carré, L. Berthier, J. Horbach, S. Ispas, and W. Kob, The Journal of chemical physics **127** (2007).
 [24] G. Molnár, P. Ganster, A. Tanguy, E. Barthel, and G. Kermouche, Acta Materialia **111**, 129 (2016).
 [25] G. Molnár, G. Kermouche, and E. Barthel, Mechanics of Materials **114**, 1 (2017).
 [26] Capital Ψ is the global value integrated over the whole volume (V), while small ψ refers to local energy densities.
 [27] B. Bourdin, J.-J. Marigo, C. Maurini, and P. Sicsic, Phys. Rev. Lett. **112**, 014301 (2014).
 [28] G. Molnár, A. Doitrand, A. Jacon, B. Prabel, and A. Gravouil, Engineering Fracture Mechanics **266**, 108390 (2022).
 [29] B. Bourdin, G. Francfort, and J.-J. Marigo, Journal of the Mechanics and Physics of Solids **48**, 797 (2000).
 [30] K. Pham, H. Amor, J.-J. Marigo, and C. Maurini, International Journal of Damage Mechanics **20**, 618 (2011).
 [31] T. Sarlat, A. Lelarge, E. Søndergård, and D. Vandembroucq, The European Physical Journal B-Condensed Matter and Complex Systems **54**, 121 (2006).
 [32] H. Kimura, K. Wada, H. Senshu, and H. Kobayashi, The Astrophysical Journal **812**, 67 (2015).
 [33] Y. Yu, N. Krishnan, M. M. Smedskjaer, G. Sant, and M. Bauchy, The Journal of chemical physics **148** (2018).
 [34] M.-C. Desjonqueres and D. Spanjaard, *Concepts in surface physics* (Springer Science & Business Media, 2012).
 [35] J. Lewandowski, W. Wang, and A. Greer, Philosophical Magazine Letters **85**, 77 (2005).

Additional material for: “How glass breaks – Damage explains the difference between surface and fracture energies in amorphous silica”

Gergely Molnár*

CNRS, INSA Lyon, LaMCoS, UMR5259, 69621 Villeurbanne, France

Etienne Barthel

Soft Matter Sciences and Engineering, CNRS, ESPCI Paris,
PSL University, Sorbonne Université, 75005 Paris, France

MODELING DETAILS

The amorphous glass samples were prepared through a random sequential placement of atoms within a periodic simulation box. Following this, molecular dynamics simulations using the LAMMPS software [S1] were conducted to equilibrate, quench, and test the samples. In this study, we examined two sample sizes: a cubic box with a side length of 100 Å, and a rectangular cuboid with dimensions of $400 \times 300 \times 100$ Å³. The sample generation methodology and the potential function employed are detailed in Ref. [S2].

After equilibration at 3000 K, the samples were quenched at a rate of 10 K/ps in an NPT ensemble to a final temperature of 10^{-5} K. The samples were then deformed in an athermal manner. Deformations were applied iteratively, with successive energy minimization steps performed using the conjugate gradient method.

Three types of simulations were conducted: (i) free surface energy calculations on the smaller sample; (ii) local elastic moduli calculations; and (iii) fracture propagation analysis on the larger sample.

To obtain the free surface energy of the material, the smaller sample was cut at different positions by displacing the atoms in a periodic environment along the y direction, and then the periodic boundary in the y direction was replaced with free surfaces. The energy of the sample was then minimized, and 2γ was calculated by dividing the energy difference by the area of the newly created surfaces: $2\gamma = \Delta\Psi_{pot}/(L_x L_z)$.

The local elastic moduli were calculated by deforming the large sample in 6 elementary ways incrementally by $\delta\epsilon = 0.01$ % until 0.5 % strain (3 compression, 3 shear). The local stresses were then correlated to local strains. This method, as used in Ref. [S2] to correlate local soft spots to sodium distributions, employs the same numerical parameters. Further details are available in the aforementioned paper.

To simulate crack propagation, the periodic boundaries in the x and y directions were removed. An initial crack with a length of 100 Å and a radius of $r_c = 10$ Å was introduced. The outer free boundaries, fixed at a distance of $H_{\text{fix}} = 15$ Å, were displaced iteratively over 4000 steps using the following K-field until $K_I = 2.2$ MPa \sqrt{m} :

$$\begin{aligned}\hat{u}_x &= \frac{K_I}{8\mu\pi} \sqrt{2\pi r} \left[(2\kappa - 1) \cos \frac{\theta}{2} - \cos \frac{3\theta}{2} \right], \\ \hat{u}_y &= \frac{K_I}{8\mu\pi} \sqrt{2\pi r} \left[(2\kappa + 1) \sin \frac{\theta}{2} - \sin \frac{3\theta}{2} \right],\end{aligned}\quad (1)$$

where r and θ are polar coordinates measured from the initial crack tip, μ is the shear modulus, $\kappa = 3 - 4\nu$, and ν is Poisson’s ratio. For the bulk sample, the elastic constants were determined as $\mu = 31.7$ GPa and $\nu = 0.25$. Note, that the largest displacement increment was smaller than 0.01 Å, which is less than 1 % of the characteristic inter-atomic distance ($r_{\text{Si-O}} = 1.61$ Å). This ensured that the applied deformation remained independent of the step size. Note, that $H_{\text{fix}} = 15$ Å is larger than the interatomic potential cutoff. A schematic illustration of the initial sample and the deformed configuration is depicted in Fig. 1a and b, with a cut in the z direction. Due to the progressively advancing crack tip K_I in our case remains a loading parameter without any significant physical meaning.

HOMOGENIZED LOCAL QUANTITIES

Local continuum quantities were computed using a physically based Gaussian convolution technique, commonly known as the coarse-graining method [S3, S4]. This method offers the advantage of conserving both energy and mass during the homogenization procedure. With this technique, homogeneous fields for displacements, displacement gradients, strains, rotations, stresses, and potential energy were obtained for both the initial (Lagrangian) and deformed (Eulerian) configurations.

To execute the convolution, the following function was employed:

$$\phi(r) = \frac{1}{w^3 \pi^{3/2}} e^{-\frac{r^2}{w^2}}, \quad (2)$$

where r is the distance between the observation point and the atom, and w is the coarse-graining width. This function is normalized such that its integral in 3D equals 1. More details about the technique can be found in Refs. [S2, S5]. An example of the coarse-grained displacement in the y direction is illustrated in Fig. 1c.

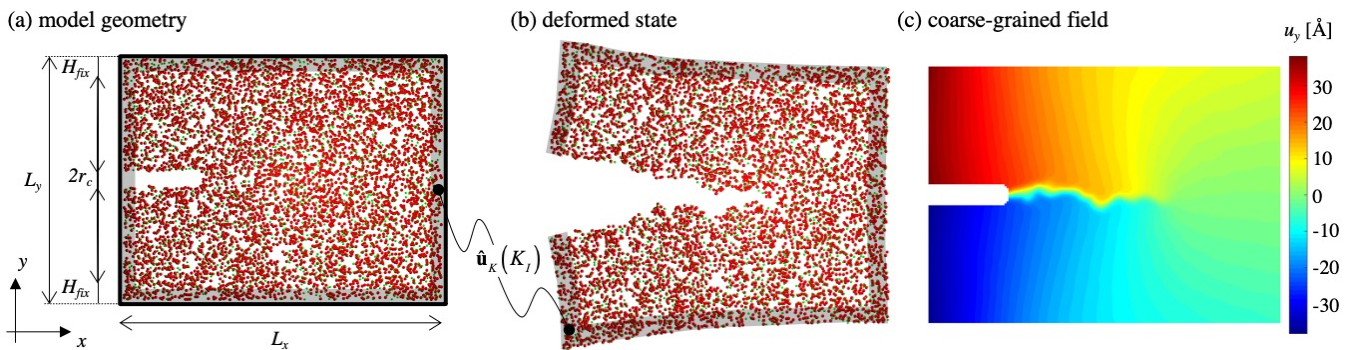


FIG. 1: (a) A cut of the atomic-scale model displaying atoms of a 5 Å thickness. (b) Deformed configuration with the same cut with $K_I = 2.2 \text{ MPa}\sqrt{m}$. (c) Coarse-grained displacement field in the Lagrangian configuration, obtained via convolution, at the same loading state as in (b).

Damage is calculated in the Lagrangian configuration following principles of solid mechanics, as most quantities are better defined in the initial state. Only Cauchy stresses needed to be interpolated back from the deformed state because coarse-graining atomic pairs in the initial configuration that were no longer in contact often resulted in locally negative strain energy, which is physically impossible. This interpolation involved displacing grid points of the Lagrangian configuration by their coarse-grained displacements, followed by interpolating stress values from the Eulerian grid to these displaced points.

To account for free surfaces in the Eulerian configuration that appear on the crack lips, a correction multiplier was defined based on the ratio of locally interpolated densities from the deformed configuration to those from the initial configuration: $\xi = \rho_L / \rho_E^{\text{int}}$. This adjustment compensates for the absence of material at the free surfaces in the deformed configuration, ensuring accurate calculations when parts of the coarse-grained volume are empty.

As amorphous materials lack the ordered structure of crystals, therefore initial local stresses can be found in the quenched material. We assume that these stresses store elastic energy, which is quantified and added to the deformation calculated during loading. The initial strain field can be calculated using linear elasticity as: $\boldsymbol{\varepsilon}_0 = \mathbf{C}^{-1}\boldsymbol{\sigma}_0$, where \mathbf{C} is the local rigidity tensor and $\boldsymbol{\sigma}_0$ is the local initial stress tensor. The initial elastic strain energy density was then obtained by $\psi_{el,0} = \frac{1}{2}\boldsymbol{\sigma}_0 : \boldsymbol{\varepsilon}_0$. We note that this quantity was significantly smaller than the energy from the applied deformation.

Damage in our case is defined by the difference between the coarse-grained elastic energy (ψ_{el}) and the undamaged energy components (ψ_0) obtained from the strain field:

$$\psi_{el}(\mathbf{u}, d) = (1 - d)^2 \psi_0^+(\boldsymbol{\varepsilon}(\mathbf{u})) + \psi_0^-(\boldsymbol{\varepsilon}(\mathbf{u})), \quad (3)$$

with d representing the damage, ψ_0^+ and ψ_0^- represent-

ing the tensile and compressive parts of the undamaged strain energy densities, to avoid damage formation in compression. We use the spectral energy decomposition [S6] here, because we found a comparable failure surface in crack free deformations than in atomic scale simulations [S7]. We recall that from simulations, the stress, strain, and local stiffness fields are available, so that ψ_0^+ and ψ_0^- can be calculated, allowing the damage to be defined as:

$$d = 1 - \sqrt{\frac{(\psi_{el} - \psi_0^-)}{\psi_0^+}}. \quad (4)$$

EFFECT OF CONVOLUTION WIDTH

One of the main findings of this Letter is the identification of an emerging length scale from molecular simulations using a Gaussian convolution. This homogenization process starts with a finite length, making it crucial to demonstrate that the results presented are essentially independent of the specific parameters used in the homogenization.

In this section, we explore how the width of the coarse-graining affects the results discussed in the main body of the article.

There are three key aspects that may be influenced by the homogenization process: (i) the elastic behavior, which indicates at what scale discrete atoms can be approximated as a continuum; (ii) the diffusion width of damage; and (iii) the effect of the free surface on local potential energy.

Our findings indicate that for a minimal length scale of $w = 8 \text{ Å}$, the elastic strain energy matches the local potential energy. This result aligns well with our previous findings on local elasticity. Additionally, we show that a width of $w = 8 \text{ Å}$ has minimal impact on damage diffusion. Lastly, we demonstrate that the free surface

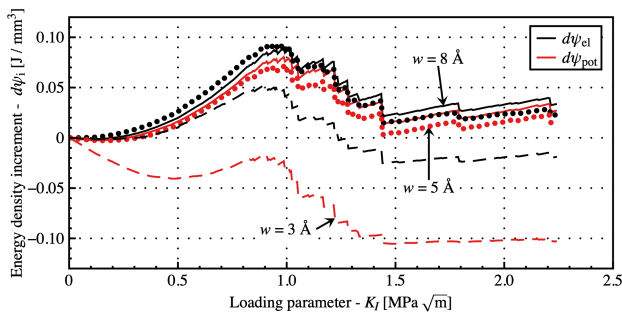


FIG. 2: Impact of coarse-graining width on local elastic and potential energy densities in the material's elastic state.

energy is highly localized on the surface, implying that while varying w may alter the local maximum amplitude, it does not affect the overall sum of the energy change. Detailed explanations are provided below.

Elasticity

Fig. 2 depicts the local strain energy density ($d\psi_{el}$) and potential energy density ($d\psi_{pot}$) in black and red, respectively. The strain energy density is calculated from the stresses and strains, while the potential energy is coarse-grained from the atomistic values. These values are shown as a function of the global loading at a position in the sample that remains elastic during deformation. The descent of the curves indicates unloading, not damage nor plasticity. Under elastic conditions, these two values are expected to match. However, as illustrated in Fig. 2, if the homogenization length is too small, neither quantity is well-defined. When calculating the surface free energy ($d\psi_{SFE} = d\psi_{pot} - d\psi_{el}$), this can result in a negative value, particularly in regions of the model where it should be zero, which is clearly not possible. Therefore, elastic analysis provides a lower bound for the coarse-graining width, which is in the range of $w = 6-8 \text{ \AA}$. We note that a similar length scale, $w = 8 \text{ \AA}$, was found where local elasticity begins to be well-defined [S2]. This was explained by micro-irreversible rearrangements present in amorphous materials even in the initial elastic stage, which are included in the slope of the experimentally measured stiffness.

Damage

While for elasticity, the larger the coarse-graining width, the better the results represent a continuum, for localized damage, it hinders the identification of the extent of the diffused damage. Fig. 3 presents the width of the damage zone in the middle plane for $K_I =$

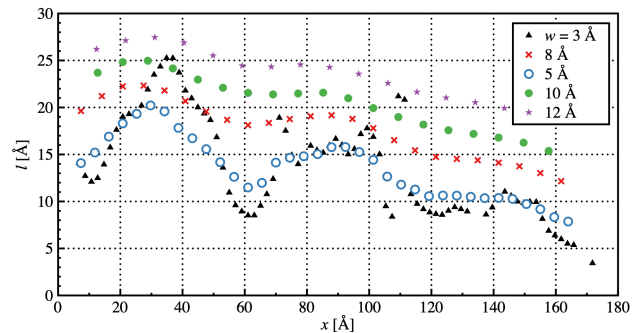


FIG. 3: Effect of coarse-graining width on the damage diffusion width at $K_I = 2.2 \text{ MPa}\sqrt{m}$ in the middle plane.

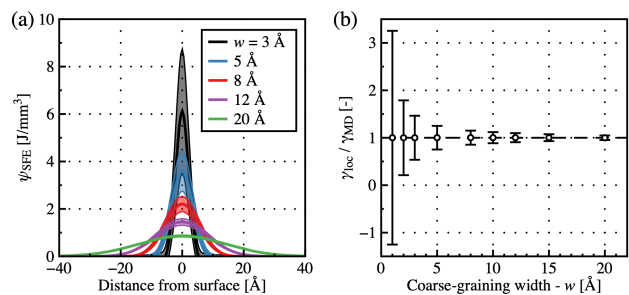


FIG. 4: Distribution of free surface energy as a function of coarse-graining width. (a) Profiles of free surface energy along the y axis for various coarse-graining widths. (b) Mean value and standard deviation of the local free surface energy γ , normalized by the global value.

$2.2 \text{ MPa}\sqrt{m}$ with various coarse-graining widths along the crack.

It is clearly visible that for $w = 3-5 \text{ \AA}$, the mean value remains the same, with only the fluctuation decreasing. At $w = 8 \text{ \AA}$, the mean value starts to increase slightly, but this increase remains within the order of 10 %. Beyond this, as w increases, the width of the damage zone, l , increases linearly.

To keep negative surface energies minimal and stresses well-defined, we accepted a slight effect on the damage diffusion and chose $w = 8 \text{ \AA}$ for subsequent analysis. It is important to note that the exact value of l might be slightly smaller. This consideration is crucial as the exact value depends on the degradation function and the phase-field description.

Surface free energy

One of the methods we used to determine the newly opened crack surface was to calculate the potential energy without elastic deformation and divide the overall

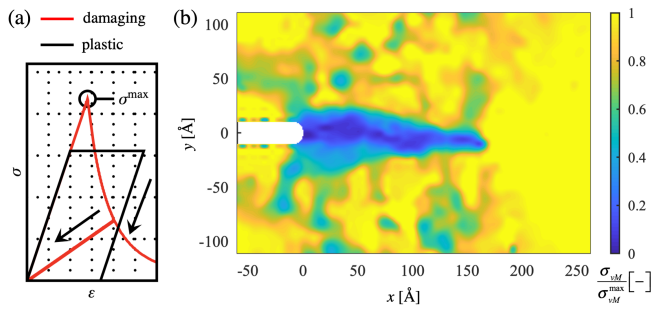


FIG. 5: (a) Principal difference between damaging and plastic response. (b) Maximum stress ratio at $K_I = 2.2 \text{ MPa}\sqrt{m}$.

sum by 2γ , the free surface energy, to find the newly opened crack surface. Interestingly, this method worked in a consistent and robust manner. However, to ensure that the homogenization length did not affect our results, we studied the energy concentration on the surface of a small sample after opening. The coarse-graining was performed on the initial coordinates to maintain continuity, and the potential energy density values displayed in Fig. 4a were shifted to the middle for easier representation.

Fig. 4a shows that as a function of coarse-graining width, the profile of $d\psi_{\text{SFE}}$ changes and reflects the coarse-graining function. This result indicates that the energy change is localized near the surface due to the loss of atomic connectivity, and this change does not diffuse into the sample. However, when integrating this change along the y axis, we recover a local 2γ , whose mean value and standard deviation are displayed in Fig. 4b, normalized by the global value without coarse-graining. It is important to observe that the mean value, and thus the overall sum, is independent of the coarse-graining width; only the finer details are lost when w is increased. Consequently, when determining the overall change in surface energy, the coarse-graining procedure does not affect the results.

LOCAL STRESS MAXIMA

There are two essential phenomenological differences between damaging and ductile behavior: (i) in damage, no plateau is reached and the stress converges to zero with loading; (ii) the elastic stiffness in damage is lost, while in plasticity it is conserved upon unloading. This is depicted in Fig. 5a.

Furthermore, to demonstrate that plastic effects are minimal during crack propagation, we present the von Mises stress divided by the maximum value throughout the entire loading process for a crack in Fig. 5b. It is evident that in the damaged zone, this ratio tends to zero, indicating damage. In contrast, if the material were duc-

tile, the ratio would have remained around 1. Furthermore, this is reinforced by the energy balance presented in the main body of the Letter, which shows that the unaccounted energies are minimal.

FINITE ELEMENT UPDATE

Finite element model updating (FEMU) [S8] was performed to identify fracture properties, such as the critical energy release rate (g_c) and the internal length scale (l_c). The objective was to update the parameters of a constitutive model so that the results of the phase-field simulation, under appropriate boundary conditions, match as closely as possible the results obtained through molecular scale simulations in the sense of a given norm. We used an AT1 description for the phase-field model with a quadratic degradation function.

The FEMU method utilizes the undamaged tensile energy (ψ_0^+) to obtain the local phase-field damage variable. The approach involves iteratively adjusting the material properties, which are considered homogeneous in this case, to minimize the difference between the damage field obtained from the ratio of damaged to undamaged energies (\mathbf{d}_{MD}) and the damage field from finite element calculations (\mathbf{d}_{FEM}).

$$\mathbf{\Lambda} = \text{argmin}[\mathbf{d}_{\text{MD}} - \mathbf{d}_{\text{FEM}}(\mathbf{\Lambda})]^T [\mathbf{d}_{\text{MD}} - \mathbf{d}_{\text{FEM}}(\mathbf{\Lambda})], \quad (5)$$

with $\mathbf{\Lambda} = [g_c \ l_c]$. The iteration is done by solving the following linear equation system:

$$\mathbf{M}\mathbf{d}\mathbf{\Lambda} = \mathbf{b}, \quad (6)$$

with

$$\begin{aligned} \mathbf{M} &= \left[\frac{\partial \mathbf{d}_{\text{FEM}}}{\partial \mathbf{\Lambda}} \right]^T \left[\frac{\partial \mathbf{d}_{\text{FEM}}}{\partial \mathbf{\Lambda}} \right], \\ \mathbf{b} &= \left[\frac{\partial \mathbf{d}_{\text{FEM}}}{\partial \mathbf{\Lambda}} \right]^T [\mathbf{d}_{\text{MD}} - \mathbf{d}_{\text{FEM}}(\mathbf{\Lambda})]. \end{aligned} \quad (7)$$

The fracture properties were changed until the maximum change in error was smaller than 10^{-6} . The procedure was executed for 20 equally spaced 2D slices in the z direction.

J-INTEGRAL

The J-integral, a contour integral, was originally proposed to deduce the energy liberated from an elastic body upon the potential advancement of a sharp crack within a homogeneous and isotropic domain. Essentially, the contour integral provides the difference between the work done on the contour and the energy stored in the solid. The resulting difference, assuming a unitary, straight,

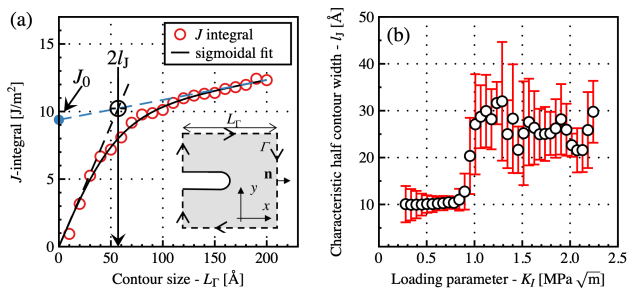


FIG. 6: (a) Schematic illustration to calculate the J-integral. (b) Characteristic half contour width as a function of loading.

horizontal crack advancement, gives the energy release rate. Its advantage at the time was that it captured the additional energy dissipated by ductile deformation and attributed it to the increment of fracture toughness. Therefore, the method is applicable in ductile cases.

In this paper, we use the J-integral to gain an approximate description and to verify the critical fracture toughness identified by the phase-field damage model.

The contour integral is defined as:

$$J = \int_{\Gamma_J} \left(\psi_{el} n_x - \mathbf{t} \frac{\partial \mathbf{u}}{\partial x} \right) d\Gamma \quad (8)$$

where $\mathbf{t} = \mathbf{P}\mathbf{n}$ with \mathbf{P} being the coarse-grained first Piola-Kirchhoff stress tensor and \mathbf{n} the normal vector to the contour.

The contour integral was centered at the local maximum of the first principal stress peak in front of the crack. Multiple contours were used, with widths denoted as L_Γ . Finally, a sigmoidal fit, which transformed into a linear function, was applied:

$$J(L_\Gamma) = \frac{J_\infty}{1 + e^{-bL_\Gamma}} + L_\Gamma c - \frac{J_\infty}{2}. \quad (9)$$

This fitting procedure is displayed in Fig. 6a.

Due to local damage and the inhomogeneous nature of the material, this contour integral is not well-defined at the crack tip. Additionally, the function exhibits a slight slope at larger contour sizes because the expected K-field is influenced by the model's boundary conditions. Therefore, the results shown in the main body of the Letter display J_0 , which is a linear interpolation of J at $L_\Gamma = 0$. Interestingly, this fit allows us to identify the length where the integral is valid and the response behaves closely to linear elastic fracture mechanics. This is done by intersecting the initial slope and the line from the final slope of eq. (9), as shown in Fig. 6a. The length l_J is displayed in Fig. 6b. It shows a similar size to where the material becomes treatable with linear elastic fracture mechanics when the contour becomes larger than the size of the diffused damaged zone.

-
- * gergely.molnar@insa-lyon.fr
- [S1] S. Plimpton, *Journal of Computational Physics* **117**, 1 (1995).
- [S2] G. Molnár, P. Ganster, J. Török, and A. Tanguy, *Journal of Non-Crystalline Solids* **440**, 12 (2016).
- [S3] R. J. Hardy, *The Journal of Chemical Physics* **76**, 622 (1982).
- [S4] I. Goldhirsch and C. Goldenberg, *The European Physics Journal E* **9**, 245 (2002).
- [S5] G. Molnár, P. Ganster, and A. Tanguy, *Physical review E* **95**, 043001 (2017).
- [S6] G. Molnár, A. Doitrand, A. Jaccon, B. Prabel, and A. Gravouil, *Engineering Fracture Mechanics* **266**, 108390 (2022).
- [S7] G. Molnár, P. Ganster, A. Tanguy, E. Barthel, and G. Kermouche, *Acta Materialia* **111**, 129 (2016).
- [S8] K. T. Kavanagh and R. W. Clough, *International Journal of Solids and Structures* **7**, 11 (1971).